

# Application of high-order lattice Boltzmann pseudopotential models

C. S. From,<sup>1,\*</sup> E. Sauret,<sup>1,†</sup> S. A. Galindo-Torres,<sup>2,3</sup> and Y.T. Gu<sup>1</sup>

<sup>1</sup>*School of Mechanical, Medical and Process Engineering, Science and Engineering Faculty,  
Queensland University of Technology, QLD 4001, Australia*

<sup>2</sup>*School of Engineering, Westlake University, Hangzhou Zhejiang Province 310024, China*

<sup>3</sup>*Institute of Advanced Technology, Westlake Institute for Advanced Study, Hangzhou Zhejiang Province 310024, China*

(Dated: May 7, 2020)

Higher-order lattice Boltzmann (LB) pseudopotential models have great potential for solving complex fluid dynamics in various areas of modern science. The discreteness of the lattice discretization makes these models an attractive choice due to their flexibility, capacity to capture hydrodynamic details and inherent adaptability to parallel computations. Despite those advantages, the discreteness makes high-order LB models difficult to apply due to the larger lattice structure, for which basic fundamental properties, namely, diffusion coefficient and contact angle, remain unknown. This work addresses this by providing general continuum solutions for those two basic properties and demonstrating these solutions to compare favorably against known theory. Various high-order LB models are shown to reproduce the sinusoidal decay of a binary miscible mixture accurately and consistently. Furthermore, these models are shown to reproduce neutral, hydrophobic and hydrophilic contact angles. Discrete differences are shown to exist, which are captured at the discrete level and confirmed through droplet shape analysis. This work provides practical tools that allow for high-order LB pseudopotential models to be used to simulate multicomponent flows.

**Introduction**—The lattice Boltzmann (LB) method provides a mesoscopic representation of fluid transport and has over the past two decades gained substantial interest in modeling complex fluid dynamics [1, 2]. Much of the success of the LB method owes to the unique lattice discretization that allows for exact advection [3], i.e., zero-numerical-diffusion, and scalable parallel computations due to the locality of computing non-linear equations on the discrete lattice allowing for highly efficient computations [4]. As the advection is exact and non-linearity is local, the LB method is an attractive alternative to numerical methods based on the Navier-Stokes equations (NSE) [5, 6]. However, the standard (low-order) lattice model, e.g., the 2D nine velocity model (Q9), is insufficient to recover the correct momentum dynamics at the NSE level [7] and violate Galilean invariance, i.e., the velocity-dependent viscosity due to cubic velocity error  $\mathcal{O}(u^3)$  [8]. Higher-order LB models are shown to completely recover the full NSE [9] and to describe hydrodynamics beyond the NSE representation [7]. This level of detail is important for fluid problems approaching nonequilibrium where nonlinearity and fluctuations due to microscopic interactions become significant [10]. Developments of high-order LB models have increasing importance as applications involving complex microscopic fluids phenomena continue to advance due to their well established potential and significance, such as microfluidics [11]. Many of these micro-applications involve complex states of fluids, i.e., fluid systems consisting of multiple components and/or phases (hereinafter referred to as multicomponent). For this reason, the development of high-order LB models for multicomponent problems is crucial for the advancement of micro-applications. Other than the greater level of hydrodynamic detail, there are two additional advantages of using these models for multicomponent problems; (1) have an inherently high-isotropy-order lattice

structure and (2) are Galilean invariant. Both of these are well known to be crucial for eliminating the spuriousness that has long plagued the LB method for multicomponent flows [12]. Surprisingly, to this date, the application of higher-order LB models for multicomponent flows remains elusive and mostly unexplored.

The LB method simulates multicomponent flows using extensions based on either the free energy [13], color-gradient model [14] or pseudopotential interactions [15]. The pseudopotential model is arguably the most popular multicomponent model [3, 6] and has consistently been used to model complex systems (see, e.g., review by Chen *et al.* [16]) including droplet dynamics on chemically patterned surfaces [17]. The pseudopotential model, although known for its simplicity, provides a unique mesoscopic representation of the underlying microscopic picture, in which non-ideal fluid mixtures are simulated by mimicking the intermolecular interactions along the lattice. It depicts intra (self) and inter (cross)-interactions discretely on the lattice by a pseudopotential  $\psi$  (a function of local density  $\rho$ ) and an amplitude  $\mathcal{G}$ , where the spatial discretization and accuracy, i.e., order of isotropy gradients, is dependent on the lattice structure used. While various high-isotropy-order lattices are available from Sbragaglia *et al.* [18] it is possible, and more convenient, to use the lattice structure of a high-order LB model directly. Different lattice structures/models incur different discrete contributions that affect the momentum flux tensor (in short, pressure tensor) [19–21]. This was first shown by Shan [22], who proposed the exact lattice theory and provided the exact discrete pressure tensor for the eighth-isotropy-order lattice structure, known as the E8. The pressure tensor of self- and cross-interactions directly influence transport properties where a direct link to the macroscopic continuum fluid equations (i.e., NSE), such as advection-diffusion, can be derived using the Chapman-Enskog analysis as shown in [23] and more recently in [24]. To derive such transport properties requires a differential form rather than a discrete form, that is, the continuum approximation (a truncation) of the discrete pressure ten-

---

\* chris.from@qut.edu.au

† emilie.sauret@qut.edu.au

sor. Shan [22], using Taylor expansion series, discovered that this continuum solution is dictated by the exact discrete form, which allows for thermodynamically consistent pseudopotential models [19, 21]. The Q9 with interactions on the E8 lattice, provided the discrete and continuum solutions by [22], has since been successfully applied to study complex fluids and assist in contributions to fundamental fluid mechanics body of knowledge. Notably, this includes the rheology of soft flowing crystals [25, 26] and evidence of stress-induced cavitation [27], which were only possible due to the extended interaction-range of the E8 over two Brillouin zones (or lattice-belts). In spite of this, the application of high-order LB models (or any other high-isotropy-order lattice structure) for any multicomponent problem has remained unexplored due to the unknown form of the exact interaction pressure tensor at both the discrete and continuum level. This was addressed in our recent work From *et al.* [21] where solutions at both levels were derived and provided in a general form for higher-order lattice structures. That includes lattice structures that involve more discrete interactions across three or more Brillouin zones (e.g., tenth-order (E10), 12th-order (E12) isotropy [18] and Q49ZOTT [21] lattice structures), allowing for even greater flexibility compared to the E8. As such, while high-order LB pseudopotential models already benefit from high-isotropy-order there is also a myriad of potential benefits offered from using such models. However, the basic properties, namely, diffusion coefficient and contact angle, required for the general application of these models for multicomponent flows remain unknown.

In this work, the high-order LB pseudopotential method detailed in From *et al.* [21] is used, for which a summary is provided in Appendix A. To address the general applicability of high-order LB pseudopotential models for multicomponent flows, the advection-diffusion equation is obtained in Sec. I to identify the diffusion coefficient,  $\mathcal{D}$ . In Sec. II the discrete solution from [21] is extended to consider fluid-structure-interactions (FSI) and the contact angle  $\theta$  is derived. Both  $\mathcal{D}$  and  $\theta$  are obtained in a general differential form that is applicable to any lattice and includes contributions from both self- and cross-interactions ( $\psi$  and  $\Psi$ ). The universality and applicability of the derived solutions are demonstrated by benchmarking three high-order LB models, the zero-one-three (ZOT) variants Q17ZOT [28] and Q25ZOT [9], and the zero-one-two-three (ZOTT) Q49ZOTT [9, 21]. In Sec. I the sinusoidal decay of binary miscible mixture is simulated and in Sec. II, a static droplet on a solid surface is simulated to demonstrate neutral, hydrophobic and hydrophilic contact angles.

## I. DIFFUSION

From a numerical point of view, diffusion transport is required to define whether two distinct fluids (denoted by superscript  $\phi$  and  $\varphi$ ) are miscible or immiscible. First, for a fluid mixture with  $\mathcal{S}$ -number of components ( $\rho = \sum_{\phi} \rho^{\phi}$ ) the

continuity of the whole fluid mixture requires

$$\partial_t \rho + \nabla \cdot (\rho \mathbf{u}) = 0, \quad (1a)$$

$$\partial_t \rho u_i + \partial_j \rho u_i u_j = -\partial_i P_o + \partial_j [\mu (\partial_j u_i + \partial_i u_j)], \quad (1b)$$

where subscript indices denote Cartesian components ( $i := x, y$ ),  $\mathbf{u}$  is the common mixture velocity [see Eq. (A4)] and  $P_o = \sum_{\phi} P_o^{\phi}$  is the total local static isotropic pressure. Each  $\phi$ -component obeys the advection-diffusion equation,

$$\partial_t \rho^{\phi} + \partial_i \rho^{\phi} u_i = -\partial_i \mathcal{D}^{\phi\varphi} \partial_i \rho^{\phi}, \quad (2)$$

where mutual diffusion between components requires the symmetry condition  $\partial_i \rho^{\phi} = -\partial_i \rho^{\varphi}$  to satisfy (1a). Equation (2) depends on the implementation of force contributions to the collision process where, in this work, force contributions are coupled explicitly using the explicit-forcing (EF) scheme [29]. This was solved recently in Küllmer *et al.* [24] but only for the case where relaxation times  $\tau^{\phi} = \tau^{\varphi}$ , self-interactions are absent, and for a standard lattice, i.e., using a continuum approximation of pressure tensor that is not general for higher-order LB models. Through Chapman-Enskog analysis using a second-order Taylor expansion [23], the EF scheme recovers the advection-diffusion [24] in the general form

$$\begin{aligned} \partial_t \rho^{\phi} + \partial_i \rho^{\phi} u_i = \\ -\partial_i \left\{ \left( \bar{\tau} - \frac{1}{2} \right) \left[ c^{\phi} \partial_i P_o + (c^{\phi} + c^{\varphi})(-c_s^2 \partial_i \rho^{\phi} + F_i^{\phi}) \right] \right\}. \end{aligned} \quad (3)$$

where  $c_s$  is the sound speed of the lattice model,  $c^{\phi}$  is the  $\phi$ -component concentration where  $c = c^{\phi} + c^{\varphi} = 1$  and the effective relaxation  $\bar{\tau} = (\rho^{\phi} \tau^{\phi} + \rho^{\varphi} \tau^{\varphi}) / \rho$  with  $\tau^{\phi}$  defined from kinematic viscosity  $\nu^{\phi} = c_s^2 (\tau^{\phi} - \frac{1}{2})$ . The mass diffusive flux of each component satisfies  $\mathbf{j}^{\phi} = \rho^{\phi} (\mathbf{u}^{\phi} - \mathbf{u}) = \mathcal{D}^{\phi\varphi} \nabla \rho^{\phi}$ .

Here, the work by Küllmer *et al.* [24] is extended by considering  $\bar{\tau}$ , all forms of interactions ( $\psi$  and  $\Psi$ ), and implementing the generalized solution to  $P_o$  and  $F_i$  into Eq. (3). Approximating the diffusion coefficient  $\mathcal{D}^{\phi\varphi}$  requires  $P_o \equiv P^{\text{tot}}$  and  $F_i^{\phi}$  to be in differential form rather than discrete [30]. This is achieved under the long-wavelength limit assumption [see 21]. The discrete form of the interaction force including all possible interactions is defined by [15] (spatial dependence is only explicitly notated in discrete equations)

$$\begin{aligned} F_i^{\phi}(\mathbf{x}) = -\psi^{\phi}(\mathbf{x}) \mathcal{G}^{\phi\phi} \sum_{\alpha} \tilde{w}_{\alpha} \psi^{\phi}(\mathbf{x} + \xi_{\alpha}) \xi_{\alpha,i} \\ -\Psi^{\phi}(\mathbf{x}) \mathcal{G}^{\phi\varphi} \sum_{\alpha} \tilde{w}_{\alpha} \Psi^{\varphi}(\mathbf{x} + \xi_{\alpha}) \xi_{\alpha,i}, \end{aligned} \quad (4)$$

where a binary mixture is considered  $\mathcal{S} = \phi, \varphi$ . Second-order Taylor expansion around  $\psi(\mathbf{x} \pm \xi_{\alpha} \Delta t)$  and  $\Psi(\mathbf{x} \pm \xi_{\alpha} \Delta t)$  in (4) results in the continuum approximation of interaction force

$$F_i^{\phi} = -C_2 \mathcal{G}^{\phi\phi} \psi^{\phi} \partial_i \psi^{\phi} - C_2 \mathcal{G}^{\phi\varphi} \Psi^{\varphi} \partial_i \Psi^{\varphi}, \quad (5)$$

where  $\Delta t = 1$  in dimensionless lattice units and the sign of  $\mathcal{G}$  defines attraction ( $-\mathcal{G}$ ) or repulsion ( $+\mathcal{G}$ ).  $C_n$  refers

to the  $n$ th-order isotropy coefficient of tensorial structures, such as second-order  $\sum_{\alpha} \tilde{w}_{\alpha} \xi_{\alpha,i} \xi_{\alpha,j} = C_2 l_{ij}$  and fourth-order  $\sum_{\alpha} \tilde{w}_{\alpha} \xi_{\alpha,i} \xi_{\alpha,j} \xi_{\alpha,k} \xi_{\alpha,l} = C_4 (l_{ij} l_{kl} + l_{il} l_{kj} + l_{ik} l_{jl})$ , where  $l$  is the identity tensor. For a given lattice  $\{w_{\alpha}, \xi_{\alpha} : \alpha = 0, 1, \dots, Q\}$ ,  $C_n$  are controlled via the interaction weights ( $\tilde{w}_{\alpha}$ ), which are  $\tilde{w}_{\alpha} \propto w_{\alpha}$  with (4) directly on the lattice. For the total pressure tensor,  $P^{\text{tot}} = P^{\text{kin}} + P^{\text{int}}$ , the kinetic contribution is obtained as the second-order moment of the equilibrium distribution  $f_{\alpha}^{\text{eq}}$  [Eq. (A3)], i.e.,  $P^{\text{kin}} \approx \sum_{\phi}^S \sum_{\alpha} f_{\alpha}^{\text{eq},\phi} \xi_{\alpha} \otimes \xi_{\alpha} = \rho c_s^2 + \rho \mathbf{u} \otimes \mathbf{u}$ , where  $\otimes$  indicates tensor product. The interaction pressure tensor ( $P^{\text{int}}$ ) due to (4) is approximated from the generalized discrete form [21], which up to second-order Taylor expansion reads

$$P^{\text{int},\phi} = \frac{C_2}{2} \left( \mathcal{G}^{\phi\phi} (\psi^{\phi})^2 + \mathcal{G}^{\phi\varphi} \Psi^{\phi} \Psi^{\varphi} \right). \quad (6)$$

Assuming  $P^{\text{kin},\phi} \equiv P^{\text{kin},\phi} \approx \rho^{\phi} c_s^2$ , at the interface where both components coexist, or for a miscible mixture, one component has a total pressure of  $P_o^{\phi} = c^{\phi} \rho^{\phi} c_s^2 + \frac{C_2}{2} \left[ \mathcal{G}^{\phi\phi} (\psi^{\phi} (c^{\phi} \rho^{\phi}))^2 + \sum_{\varphi \neq \phi}^S \mathcal{G}^{\phi\varphi} \Psi^{\phi} (c^{\varphi} \rho^{\varphi}) \Psi^{\varphi} (c^{\varphi} \rho^{\varphi}) \right]$ , where the total pressure is  $P^{\text{tot}} = \sum_{\phi}^S P_o^{\phi}$ . Furthermore, if the two components in the mixture are completely immiscible then  $\Psi^{\phi} \cdot \Psi^{\varphi} \approx 0$  and, as such, in the bulk of each component the total pressure is

$$P_o^{\phi} = \rho^{\phi} c_s^2 + \frac{C_2}{2} \mathcal{G}^{\phi\phi} (\psi^{\phi})^2. \quad (7)$$

$P^{\text{int}}$  (6) is truncated up to second-order isotropy gradients, which intrinsically assumes the tensor to be completely isotropic, hence a scalar quantity. Realistically, the pressure tensor at the interface is anisotropic, which requires at least fourth-order isotropy gradients [18]. Equations (5) and (6) are practical estimates and subbed into (3) to derive the diffusion coefficient ( $\mathcal{D}^{\phi\varphi}$ ). Since potentials are functions of local density it is possible to use identities  $\partial_i \psi = \partial_{\rho} \psi \times \partial_i \rho$  and after factoring out  $\partial_i \rho^{\phi}$  to conform with the advection-diffusion equation (2) where  $\mathcal{D}^{\phi\varphi}$  is then defined by

$$\mathcal{D}^{\phi\varphi} = \left( \bar{\tau} - \frac{1}{2} \right) \times \left[ C_2 \left( \mathcal{G}^{\phi\varphi} \left[ c^{\phi} \Psi^{\varphi} \Psi'^{\phi} + c^{\varphi} \Psi^{\phi} \Psi'^{\varphi} \right] - c^{\phi} \mathcal{G}^{\varphi\varphi} \psi^{\varphi} \psi'^{\varphi} - c^{\varphi} \mathcal{G}^{\phi\phi} \psi^{\phi} \psi'^{\phi} \right) - c_s^2 (c^{\phi} + c^{\varphi}) \right], \quad (8)$$

where  $\psi' = d\psi/d\rho$ ,  $\Psi' = d\Psi/d\rho$ , and, symmetry requires  $\partial_i \rho^{\phi} = -\partial_i \rho^{\varphi}$  and  $\mathcal{G}^{\phi\varphi} = \mathcal{G}^{\varphi\phi}$ . The miscible,  $\mathcal{D}^{\phi\varphi} < 0$ , and immiscible,  $\mathcal{D}^{\phi\varphi} > 0$ , regimes are given by a critical limit for the mutual interaction strength defined by solving Eq. (8) for  $\mathcal{D}^{\phi\varphi} = 0$ ,

$$G_{\text{crit}}^{\phi\varphi} = \frac{c_s^2 (c^{\phi} + c^{\varphi}) + C_2 (c^{\phi} \mathcal{G}^{\varphi\varphi} \psi^{\varphi} \psi'^{\varphi} + c^{\varphi} \mathcal{G}^{\phi\phi} \psi^{\phi} \psi'^{\phi})}{C_2 (c^{\phi} \Psi^{\varphi} \Psi'^{\phi} + c^{\varphi} \Psi^{\phi} \Psi'^{\varphi})}. \quad (9)$$

Defining  $\mathcal{G}^{\phi\varphi} = C \cdot G_{\text{crit}}^{\phi\varphi}$  allow two components to be set as miscible or immiscible by  $C < 1$  or  $C > 1$ , respectively. By imposing certain conditions it is possible to reduce and simplify the generalized solution (9). Firstly, setting the second-order

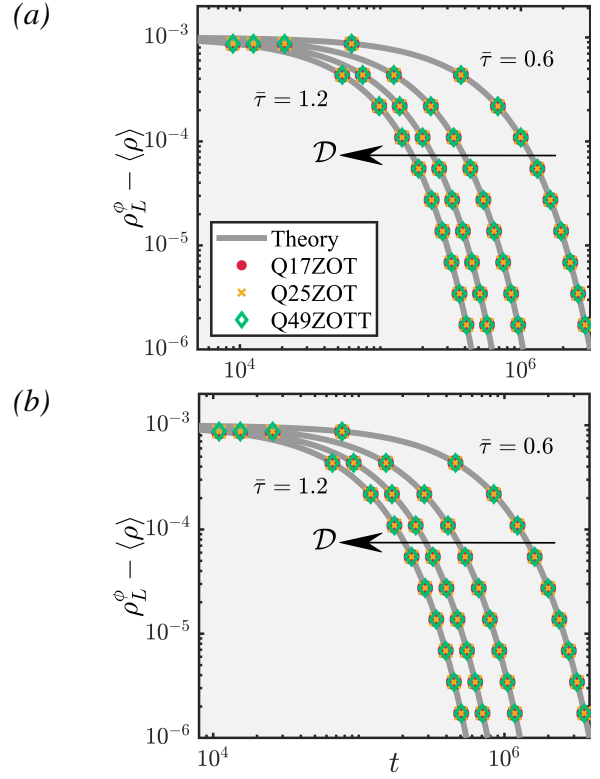


**FIG. 1:** Sinusoidal decay of a miscible binary mixture where the theoretical solution [Eq. (B1)] (solid line) is compared against the Q17ZOT (●), Q25ZOT (×) and Q49ZOTT (◇). (a) only cross-interactions to complement known solution (10) and (b) all interactions are included to complement derived full solution (8) and (9). All lattice models were run near the critical limit  $G^{\phi\varphi}/G_{\text{crit}}^{\phi\varphi} = 0.9$  for  $\bar{\tau} = \{1.2, 1.0, 0.8, 0.6\}$  (in order of appearance from left to right).

isotropy coefficient to  $C_2 = c_s^2$  (possible by setting interaction weights  $\tilde{w}_{\alpha}$  to be equal to the lattice weights  $w_{\alpha}$ ) allows the critical limit  $G_{\text{crit}}^{\phi\varphi}$  (9), for a given problem, to be the same regardless of the lattice model. However,  $\mathcal{D}^{\phi\varphi}$  still depends on  $c_s$  as seen in (8). In addition, if the concentration of each component at the interface is  $c^{\phi} = c^{\varphi} = 1/2$  and self-interactions are neglected then (9) further reduces to

$$G_{\text{crit}}^{\phi\varphi} = 2(\Psi^{\varphi} \Psi'^{\phi} + \Psi^{\phi} \Psi'^{\varphi})^{-1}, \quad (10)$$

which is the same form given in [24]. Notice that, unlike traditional force-schemes [23], with the EF scheme  $G_{\text{crit}}^{\phi\varphi}$  (9) is independent of  $\bar{\tau}$ , as reported in [24] for (10).

To demonstrate the universality and applicability of derived solution for  $\mathcal{D}^{\phi\varphi}$  (8) the accuracy across various high-order lattices is tested numerically using the popular decaying sinusoidal wave of a miscible ( $\mathcal{D}^{\phi\varphi} < 0$ ) binary mixture (details of the known theoretical solution and initialization are provided in Appendix B 1). Simulations are conducted on a grid ( $n_x = 200$ ,  $n_y = 4$ ), with an initial perturbation of  $\delta = 10^{-3}$  and run until the local  $\phi$ -density  $\rho_L^{\phi} = \rho^{\phi}(\frac{1}{2}n_x, t)$  satisfies  $\rho_L^{\phi} - \langle \rho \rangle = 10^{-6}$  [Fig. 1]. Three high-order LB models are benchmarked, Q17ZOT, Q25ZOT, and Q49ZOTT, where interactions (4) are deployed directly on their respective lat-

tice structure and the interaction weights  $\tilde{w}_\alpha$  are scaled so that  $C_2 = 1$  and  $C_4 = c_s^2$  by setting  $\tilde{w}_\alpha = w_\alpha/c_s^2$ . The sound speed  $c_s$  of the Q49ZOTT model has been rescaled to match that of the ZOT lattices [see 21] to avoid ambiguity in dimensionless scaling. These three lattice models differ in terms of

- contributions at the discrete level, that is, interaction forces (4) are computed on different lattice links with different magnitudes.
- Q17ZOT and Q25ZOT have the same order of isotropy (spatial accuracy) whereas Q49ZOTT is two orders more accurate allowing for discrete contributions to be assessed and the uniqueness of isotropy-order to be tested.
- Q17ZOT and Q25ZOT recover up to third-order terms in the equilibrium distribution, compared to Q49ZOTT which can recover up to fourth-order terms [see Eq. (A3)].

The general fourth-order-isotropy pseudopotential that satisfies thermodynamic consistency [19] is used for both self- and cross-interactions (for demonstrative purposes), i.e.,  $\psi^\phi = [\rho^\phi / (\epsilon + \rho^\phi)]^{1/\epsilon}$  and  $\Psi^\phi = [\rho^\phi / (\epsilon + \rho^\phi)]^{1/\epsilon}$ , respectively, where  $\epsilon = (6C_4 - 2C_2)/(6C_4 + C_2)$  [21].

In Figure 1a, only cross-interactions are considered to complement the known solution (10). In Figure 1b, all forms of interactions are included where self-interactions ( $\mathcal{G}^{\phi\phi}$  and  $\mathcal{G}^{\varphi\varphi}$ ) were chosen so that the bulk pressure of each component is  $P_0^\phi/(c_s^2\rho^\phi) = 0.9$  using Eq. (7). In all simulations cross-interaction strength is set close to the critical limit  $\mathcal{G}^{\phi\varphi}/\mathcal{G}_{crit}^{\phi\varphi} = 0.9$  where  $\mathcal{D}^{\phi\varphi}$  is arbitrarily close to zero. The results between the three lattice models and theoretical solution

are indistinguishable, which validates the derived general solution for the diffusion coefficient (9). The accuracy is further appreciated by the consistency between lattice models, all of which involve different discrete force contributions, across the extremely long advection times ( $>> 10^5$  numerical steps in time were required to meet the criteria  $\rho_L^\phi - \langle \rho \rangle \leq 10^{-6}$ ). This demonstrates the universality of the solution and the robust application of higher-order LB pseudopotential models.

## II. CONTACT ANGLE

Hydrophilic, hydrophobic, or, neutral surfaces, quantified by the contact angle, are important for a wide range of applications, from porous media to modern surface technology in self-cleaning surfaces. These surfaces are the result of the interactions of different fluid components with the solid boundary ( $\mathbf{x}^w$ ), i.e., FSI, which is modeled directly with the pseudopotential model [31] by readapting Eq. (4)

$$F_i^{w,\phi}(\mathbf{x}) = -\psi^\phi(\mathbf{x})\mathcal{G}^{w\phi} \sum_{\alpha} \tilde{w}_\alpha \psi^{w,\phi}(\mathbf{x} + \xi_\alpha) \xi_{\alpha,i}, \quad (11)$$

where  $\psi^{w,\phi}$  is the potential-density of the solid boundary at  $\mathbf{x}^w$  and unless  $(\mathbf{x} + \xi_\alpha) \in \mathbf{x}^w$  this potential is set to zero.  $\psi^{w,\phi}$  is set to equal the initial density of each respective component. It is assumed that FSI scale linearly with density gradients, which can be imposed by  $\mathcal{G}^{w\phi}\psi^\phi(\mathbf{x}) := \mathcal{G}^{w\phi}\rho^\phi(\mathbf{x})$ ,  $\forall \mathbf{x}$ . Within the vicinity of the solid boundary  $(\mathbf{x} + \xi_\alpha) \in \mathbf{x}^w$  the total pressure tensor has to account for these interactions [i.e., FSI (11)] and is now defined by  $P^{\text{tot}} = P^{\text{kin}} + P^{\text{int}} + P^w$ . A discrete form of pressure tensor  $P^w$  due to FSI (11) has not been previously defined in the literature. With the discrete form of  $P^{\text{int}}$  addressed in [21] it is straightforward to recast this discrete form to account for FSI (11),

$$\begin{aligned} P_{ij}^{w,\phi}(\mathbf{x}) = \sum_z \mathcal{P}_{ij}^{w,\phi(z)}(\mathbf{x}) = & \left\{ \sum_{\alpha} \frac{\tilde{w}_\alpha}{2\mathcal{E}^z} \left[ \mathcal{G}^{w\phi}\psi^\phi(\mathbf{x}) \cdot \psi^{w,\phi}(\mathbf{x} + \xi_\alpha) \xi_{\alpha,i} \xi_{\alpha,j} \right] \right. \\ & + \sum_{\alpha} \sum_{\beta}^{\epsilon_{\beta}^{\bar{z}} = \mathbf{N}^{\bar{z}}} \frac{\tilde{w}_\alpha}{2\mathcal{E}^{\bar{z}}} \left[ \mathcal{G}^{w\phi}\psi^\phi(\mathbf{x} + \epsilon_{\beta}^{\bar{z}}) \cdot \psi^{w,\phi}(\mathbf{x} - \xi_\alpha + \epsilon_{\beta}^{\bar{z}}) \xi_{\alpha,i} \xi_{\alpha,j} \right] \\ & \left. + \sum_{\alpha} \sum_{\beta}^{\epsilon_{\beta}^{\hat{z}} = \mathbf{N}^{\hat{z}}} C_{\beta} \frac{\tilde{w}_\alpha}{2\mathcal{E}^{\hat{z}}} \left[ \mathcal{G}^{w\phi}\psi^\phi(\mathbf{x} + \epsilon_{\beta}^{\hat{z}}) \cdot \psi^{w,\phi}(\mathbf{x} - \xi_\alpha + \epsilon_{\beta}^{\hat{z}}) \xi_{\alpha,i} \xi_{\alpha,j} \right] \right\}, \end{aligned} \quad (12)$$

where superscript  $z$ ,  $\bar{z}$  and  $\hat{z}$  denote symmetry groups uniquely defined by  $z = |\xi_1|^2, |\xi_2|^2 \dots |\xi_\alpha|^2$  where the two unique symmetry groups  $\bar{z}, \hat{z} \in z > 2$ , i.e., lattice  $\xi_\alpha$  that span beyond the first Brillouin zone. More specifically,  $\bar{z}$ -group considers all vectors ( $\xi_\alpha^z \forall z = \bar{z}$ ) that are purely axial,  $\xi_{\alpha,i} \cdot \xi_{\alpha,j} = 0, i \neq j$ , or purely diagonal,  $|\xi_{\alpha,i}| = |\xi_{\alpha,j}|$ . Symmetry group  $\hat{z}$  considers all vectors ( $\xi_\alpha^z \forall z = \hat{z}$ ) that consists of diagonal vectors with mixed components,  $\xi_{\alpha,i} \neq \xi_{\alpha,j}$  and  $\xi_{\alpha,i}, \xi_{\alpha,j} \neq 0$ . The

second and third line in (12) allows for all  $\bar{z}$  and  $\hat{z}$  contributions to be accounted for, where technical details of the parameters; scalars  $\mathcal{E}$  and  $C_\beta$ , and, vectors  $\epsilon_\beta$  and  $\mathbf{N}$ , were introduced in From *et al.* [21] and the following will provide a brief summary.  $\mathcal{E}^z$  is the largest absolute value of the components in the lattice velocity, defined by:  $\mathcal{E}^z = \max_{\alpha}(|\xi_\alpha^z|)$ ,  $\forall \alpha \in \xi_\alpha^z$ . In symmetry groups  $\bar{z}$  and  $\hat{z}$  there exist  $\beta = 1, \dots, (\mathcal{E}^z - 1)$  additional contributions that are not captured by  $\mathbf{x} + \xi_\alpha$  [i.e., the first



line in (12)]. These additional contributions are accounted for at the discrete level by  $\mathbf{x} - \xi_\alpha^z + \varepsilon_\beta^z$  with the introduction of the vector  $\varepsilon_\beta^z : \beta = 1, \dots, (\mathcal{E}^z - 1)$ . Initially, this is set to the directional unit vector ( $\varepsilon_{\beta=1} = \mathbf{U}_\alpha$ ), which is given by  $\mathbf{U}_\alpha(\xi_\alpha) = \mathbf{1} \circ \text{sgn}(\xi_\alpha)$  where  $\mathbf{1}$  is a constant unit vector,  $\text{sgn}(\cdot)$  denotes signum function and  $\circ$  denotes Hadamard product. Then,  $\varepsilon_{\beta>1}$  progressively shifts ( $\varepsilon_\beta = \varepsilon_{\beta-1} + \mathbf{U}_\alpha$ ) towards  $\mathbf{N}^z$  until  $\varepsilon_{\beta=\text{end}}^z = \mathbf{N}^z$ , where the vector  $\mathbf{N}(\xi_\alpha) = (\mathcal{E} - 1)\mathbf{U}_\alpha$  provided that  $\varepsilon_{\beta-1,i} \neq \xi_{\alpha,i}$  for any  $i$ th component; otherwise  $\varepsilon_{\beta,i} = \varepsilon_{\beta-1,i}$ . Lastly,  $C_\beta$  is required *only* for  $\hat{z} = 13$  and any other symmetry group  $\hat{z} < 13$  this factor is set to unit constant. For  $\hat{z} = 13$ , during the sum over  $\beta$  this factor is initially set to  $C_{\beta=1} = 3/2$  and then  $C_{\beta=(3-1)} = 1/2$ . For full details refer to [21]. The interaction pressure tensor due to FSI (11) is now defined in a generalized discrete form (12) and comes in addition to the discrete solutions presented in [21].

At the three-phase-interface (two fluid components, or phases, and the solid phase) the contact angle can be deter-

mined from Young's equation [32],

$$\cos \theta = \frac{\sigma^{\text{w}\phi} - \sigma^{\text{w}\varphi}}{\sigma^{\phi\varphi}}, \quad (13)$$

for which the droplet is phase- $\phi$  rich and the surrounding fluid is phase- $\varphi$  rich. In (13)  $\sigma^{\text{w}\phi}$  (and  $\sigma^{\text{w}\varphi}$ ) is the tension between the solid boundary and each fluid component due to FSI (11) and  $\sigma^{\phi\varphi}$  is the interfacial tension between binary fluids. These are defined by [33] (in the case where the surface boundary is normal to principle  $y$ -axis)

$$\begin{aligned} \sigma^{\phi\varphi} &= \int_{\phi\varphi} (P_{yy}^{\text{tot}} - P_{xx}^{\text{tot}}) dy, \\ \text{and } \sigma^{\text{w}\phi} &= \int_{\text{w}\phi} (P_{yy}^{\text{tot},\phi} - P_{xx}^{\text{tot},\phi}) dy, \end{aligned} \quad (14)$$

which can be evaluated given (12) and the solutions in [21] allowing the contact angle (13) to be solved at the discrete level. Furthermore, it was shown in [21], with  $\mathbf{P}^{\text{int}}$  truncated at fourth-order isotropy gradients, that at the continuum level  $\sigma^{\phi\varphi}$  will only depend on  $\mathcal{C}_4$ , despite an arbitrary number of interactions (4) at the discrete level. The continuum approximation of  $\sigma^{\text{w}\phi}$  can be obtained similarly to  $\sigma^{\phi\varphi}$  following From *et al.* [21], where in this case all gradients are directed in  $y$ , i.e.,

$$\sigma^{\text{w}\phi} \approx -\frac{\mathcal{C}_4}{2} \mathcal{G}^{\phi\phi} \int_{\text{w}\phi} (\partial_y \psi^\phi)^2 dy - \frac{\mathcal{C}_4}{2} \mathcal{G}^{\text{w}\phi} \int_{\text{w}\phi} \partial_y \psi^{\text{w},\phi} \partial_y \psi^\phi dy - \frac{\mathcal{C}_4}{2} \mathcal{G}^{\phi\varphi} \int_{\text{w}\phi} \partial_y \Psi^\phi \partial_y \Psi^\varphi dy \quad (15)$$

With the continuum form of  $\sigma^{\phi\varphi}$  and  $\sigma^{\text{w}\phi}$  it is possible to define (13) at the continuum level explicitly by (see, e.g., Benzi *et al.* [33])

$$\cos \theta \approx \frac{\frac{\mathcal{C}_4}{2} \left[ \left( \mathcal{G}^{\varphi\varphi} \int_{\text{w}\varphi} |\partial_y \psi^\varphi|^2 dy + \mathcal{G}^{\text{w}\varphi} \int_{\text{w}\varphi} |\partial_y \psi^{\text{w},\varphi} \partial_y \psi^\varphi| dy \right) - \left( \mathcal{G}^{\phi\phi} \int_{\text{w}\phi} |\partial_y \psi^\phi|^2 dy + \mathcal{G}^{\text{w}\phi} \int_{\text{w}\phi} |\partial_y \psi^{\text{w},\phi} \partial_y \psi^\phi| dy \right) \right]}{\mathcal{C}_4 \left[ \frac{1}{2} \mathcal{G}^{\varphi\varphi} \int_{\varphi\varphi} (\partial_y \psi^\varphi)^2 dy + \frac{1}{2} \mathcal{G}^{\phi\phi} \int_{\phi\phi} (\partial_y \psi^\phi)^2 dy + \mathcal{G}^{\phi\varphi} \int_{\phi\varphi} \partial_y \Psi^\phi \partial_y \Psi^\varphi dy \right]}, \quad (16)$$

which is a fourth-order-isotropy truncation inherited from (15). Note that the cross-interactions terms in  $\sigma^{\text{w}\phi}$  and  $\sigma^{\text{w}\varphi}$  cancel out. In the absence of self-interactions, and factoring out dependence on  $\mathcal{C}_4$ , Eq. (16) reduces to

$$\cos \theta \approx \frac{\mathcal{G}^{\text{w}\varphi} \int_{\text{w}\varphi} |\partial_y \psi^{\text{w},\varphi} \partial_y \psi^\varphi| dy - \mathcal{G}^{\text{w}\phi} \int_{\text{w}\phi} |\partial_y \psi^{\text{w},\phi} \partial_y \psi^\phi| dy}{2 \mathcal{G}^{\phi\varphi} \int_{\phi\varphi} \partial_y \Psi^\phi \partial_y \Psi^\varphi dy}, \quad (17)$$

which is the same simplified form as in Benzi *et al.* [33]. From this, it is straightforward to identify that if  $\mathcal{G}^{\text{w}\varphi} = \mathcal{G}^{\text{w}\phi}$  and  $\partial_y \psi^{\text{w},\varphi} \partial_y \psi^\varphi = \partial_y \psi^{\text{w},\phi} \partial_y \psi^\phi$ , then, theoretically, the contact angle  $\theta = \arccos(0) = 90^\circ$  for any  $\mathcal{G}^{\phi\varphi}$  in the absence of self-interactions.

The contact angle is tested by simulating a static droplet on a flat surface (details in Appendix B 2) where similarly

to the sinusoidal decay in Sec. I, the Q17ZOT, Q25ZOT and Q49ZOTT are used with isotropy coefficients set to  $\mathcal{C}_2 = 1$  and

$C_4 = c_s^2$ . The potentials used are  $\psi^\phi = [\rho^\phi / (\epsilon + \rho^\phi)]^{1/\epsilon}$  and  $\Psi^\phi = \rho^\phi$ . It is reminded that  $\mathcal{G}^{\text{w}\phi}\psi^\phi(\mathbf{x}) := \mathcal{G}^{\text{w}\phi}\rho^\phi(\mathbf{x})$ ,  $\forall \mathbf{x}$  in Eqs. (11) and (12). Given  $\psi$ ,  $\Psi$  and the isotropy coefficients (controlled via  $\tilde{w}_\alpha$ ) it is possible to solve for  $\mathcal{D}^{\phi\varphi} = 0$  to obtain  $G_{\text{crit}}^{\phi\varphi}$  [Eq. (9)] and set  $\mathcal{G}^{\phi\varphi} = C \cdot G_{\text{crit}}^{\phi\varphi}$  with  $C > 1$  to simulate an immiscible binary mixture. For validation, a qualitative comparison is insufficient as the actual contact angle may be visually deceiving. In this work, validation is achieved by comparing the contact angle at the discrete level ( $\theta_N$ ) directly against two additional approaches based on the droplet shape analysis, denoted by  $\theta_{\text{geo}}$  and  $\theta_{\text{FIT}}$ . The various solutions to the contact angle are:

- $\theta_N$  — calculated using the discrete solution (12) directly to evaluate surface tensions (14) and then Young's equation (13).
- $\theta_{\text{geo}}$  — the contact angle has a known approximation assuming a spherical cap shape [34],  $\theta_{\text{geo}} = \arctan[2(H - R_0)/L] + \pi/2$  with  $R_0 = (L^2 + 4H^2)/(8H)$ , where  $L$  and  $H$  are the droplet length on the boundary and height, respectively.
- $\theta_{\text{FIT}}$  — obtained from direct double-elliptic fitting of the droplet shape using an open-source code from Andersen and Taboryski [35], which was modified to allow for the density field from the numerical data to be used directly (by converting  $\rho^\phi(\mathbf{x})$  into an unsigned 8-bit integer).

All these solutions require the exact three-phase-interface point-of-contact located at the first fluid-node where  $c^\phi = c^\varphi = 1/2$ , shown as a green-circle marker in Fig. 2.

The known theoretical solution of the contact angle  $\theta = 90^\circ$  (17), i.e., neutral contact angle, is tested by setting self-interactions to zero and boundary-interactions to be equal  $\mathcal{G}^{\text{w}\phi} = \mathcal{G}^{\text{w}\varphi}$ . Figure 2a shows that  $\theta_N$  (12) and (14) is in exact agreement with the theoretical requirement  $\theta = 90^\circ$ , whereas  $\theta_{\text{FIT}}$  deviates slightly ( $\pm 3^\circ \sim 4^\circ$ ) and  $\theta_{\text{geo}}$  shows the largest deviation ( $> 7^\circ$ ). The deviations for the geometric-based solutions,  $\theta_{\text{FIT}}$  and  $\theta_{\text{geo}}$ , are most likely owed to their dependence on spatial resolution [34]. Furthermore, in Figs. 2b and 2c boundary-interactions are set to equal-opposite  $\mathcal{G}^{\text{w}\phi} = -\mathcal{G}^{\text{w}\varphi}$ , which allows for hydrophobic  $\theta > 90^\circ$  [2b] or hydrophilic  $\theta < 90^\circ$  [2c] fluid-solid dynamics to be modeled by setting  $+\mathcal{G}^{\text{w}\phi}$  or  $-\mathcal{G}^{\text{w}\phi}$ , respectively. Both  $\theta_{\text{FIT}}$  and  $\theta_N$  are in excellent agreement with each other and qualitatively match the contour plot. In contrast,  $\theta_{\text{geo}}$  fails to adequately match the simulated results at a qualitative level. However,  $\theta_{\text{geo}}$  does allow for hydrophobic [2b] and hydrophilic [2c] contact angles to be identified. Interestingly, for each test case  $\theta_{\text{geo}}$  remains constant across all lattice models, whereas both  $\theta_{\text{FIT}}$  and  $\theta_N$  indicate minuscule differences between lattice models for the hydrophobic [2b] and hydrophilic [2c] cases. These are due to differences at the discrete lattice level and as such, it is reasonable to expect  $\theta_N$  to identify such differences. It is, however, more important and interesting to note that

differences are also identified by the double-elliptic fitting ( $\theta_{\text{FIT}}$ ), which suggests that the  $\theta_N$  results are not the product of 'random' numerical-noise. Instead,  $\theta_{\text{FIT}}$  complements the discrete  $\theta_N$  solution by identifying that, other than the droplet length and height (evident by the constant  $\theta_{\text{geo}}$ ), the quasi-equilibrium droplet-shapes themselves differ between lattice models. Such discrete differences are considered as an attribute of isotropy-order of different lattice structures. For this reason, it is surprising that the Q17ZOT and Q25ZOT differ at this quasi-equilibrium state, since both, although different at the discrete level, theoretically have the same order of accuracy for both isotropy-gradients and the equilibrium distribution [see Eq. (A3)]. Nevertheless, the results presented in Fig. 2 collectively validate the generalized continuum approximation for the contact angle (16) and the newly proposed discrete solution (12) for the interaction pressure tensor due to FSI (11).

### III. SUMMARY AND CONCLUSIONS

To further broaden the applicability of higher-order LB pseudopotential models, generalized solutions of the diffusion coefficient and contact angle were addressed. A generalized diffusion equation was derived and validated by comparison against the theoretical solution for a sinusoidal decay of a binary miscible mixture. To demonstrate the universality and applicability of the derived solution, all simulations were carried out with the Q17ZOT, Q25ZOT, and Q49ZOTT. To address the contact angle, first, the generalized discrete pressure tensor from [21] was extended to consider FSI. Then, the generalized continuum form of the interface tension was defined and with Young's equation, a continuum approximation of the contact angle was derived. By simulating a static droplet on a flat surface numerical validation was achieved for neutral, hydrophobic and hydrophilic surfaces. The exact discrete form was shown to identify differences between the three high-order lattices, which were found to exist even between Q17ZOT and Q25ZOT despite conforming to the same order of isotropy gradients. The exact implications of these discrete differences, in terms of accuracy and stability, are yet to be investigated in detail. The ability to obtain this exact knowledge at the discrete level will, therefore, play an essential role in future developments. In particular, the impact of accuracy and stability of different high-order LB models for multicomponent flows are of great interest.

Addressing the diffusion coefficient and contact angle is a significant advancement in the field of higher-order LB pseudopotential models by allowing such models to be readily and more conveniently applied for general multicomponent problems. The exact discrete solution and the practical, continuum approximation are now both available. The latter allows for these models to be readily and more conveniently applied while the former provides the exact information of discrete contributions, which is important for future developments.

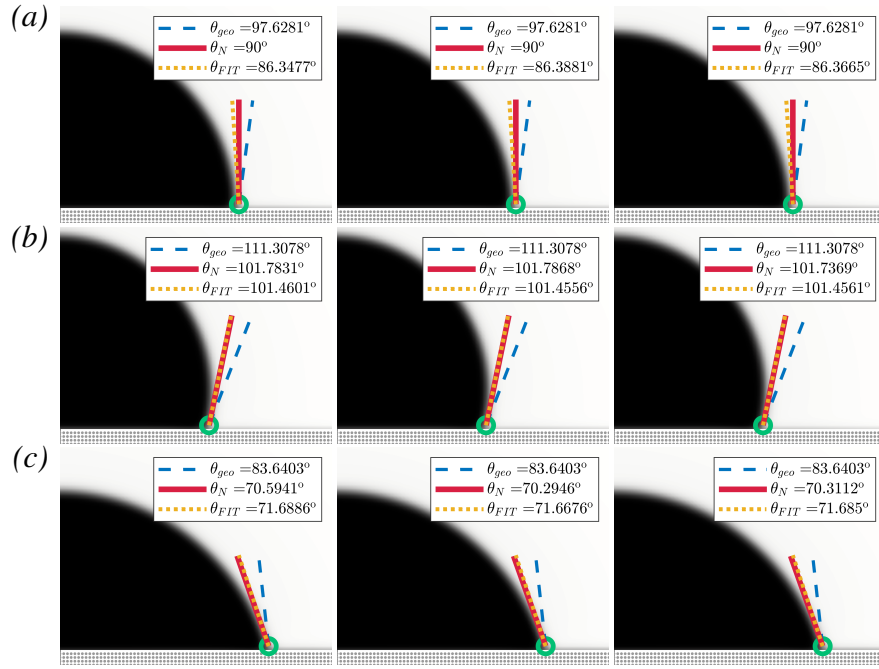


**FIG. 2:** Static droplet on a flat surface simulated with Q17ZOT (left), Q25ZOT (middle) and Q49ZOTT (right), including all interactions. (a) neutral case where boundary-interactions are equal ( $G^{w\phi} = G^{w\psi}$ ) and the contact angle theoretically reduces to  $\theta = 90^\circ$ . (b) hydrophobic and (c) hydrophilic cases where boundary-interactions are set to equal-opposite ( $G^{w\phi} = -G^{w\psi}$ ). The green marker pinpoints the exact three-phase-interface point-of-contact. All plots are cropped at  $x = [\frac{1}{2}n_x : \frac{7}{8}n_x]$  and  $y = [1 : \frac{3}{8}n_y]$ .

- 
- [1] C. Aidun and J. Clausen, *Annual Review of Fluid Mechanics* **42**, 439 (2010).
  - [2] U. D. Schiller, T. Krüger, and O. Henrich, *Soft Matter* **14**, 9 (2018).
  - [3] S. Succi, *The lattice Boltzmann Equation: For Complex States of Flowing Matter* (Oxford University Press, 2018).
  - [4] M. Bernaschi, S. Melchionna, and S. Succi, *Rev. Mod. Phys.* **91**, 025004 (2019).
  - [5] H. Chen, S. Kandasamy, S. Orszag, R. Shock, S. Succi, and V. Yakhot, *Science* **301**, 633 (2003).
  - [6] T. Krüger, H. Kusumaatmaja, A. Kuzmin, O. Shardt, G. Silva, and E. M. Viggen, *The lattice Boltzmann Method: Principles and Practice*, 1st ed. (Springer Int. Publishing, 2017) pp. 978–3.
  - [7] X. Shan, X.-F. Yuan, and H. Chen, *J. Fluid Mech.* **550**, 413 (2006).
  - [8] Y. H. Qian and S. A. Orszag, *Europhysics Letters (EPL)* **21**, 255 (1993).
  - [9] S. S. Chikatamarla and I. V. Karlin, *Phys. Rev. E* **79**, 046701 (2009).
  - [10] M. Torrilhon, *Annual Review of Fluid Mechanics* **48**, 429 (2016).
  - [11] G. Whitesides, *Nature* **442**, 368 (2006).
  - [12] X. Shan, *Phys. Rev. E* **73**, 047701 (2006).
  - [13] M. R. Swift, W. R. Osborn, and J. M. Yeomans, *Phys. Rev. Lett.* **75**, 830 (1995).
  - [14] A. K. Gunstensen, D. H. Rothman, S. Zaleski, and G. Zanetti, *Phys. Rev. A* **43**, 4320 (1991).
  - [15] X. Shan and H. Chen, *Phys. Rev. E* **47**, 1815 (1993).
  - [16] L. Chen, Q. Kang, Y. Mu, Y.-L. He, and W.-Q. Tao, *International Journal of Heat and Mass Transfer* **76**, 210 (2014).
  - [17] S. Varagnolo, D. Ferraro, P. Fantinel, M. Pierro, G. Mistura, G. Amati, L. Biferale, and M. Sbragaglia, *Phys. Rev. Lett.* **111**, 066101 (2013).
  - [18] M. Sbragaglia, R. Benzi, L. Biferale, S. Succi, K. Sugiyama, and F. Toschi, *Phys. Rev. E* **75**, 026702 (2007).
  - [19] M. Sbragaglia and X. Shan, *Phys. Rev. E* **84**, 036703 (2011).
  - [20] M. Sbragaglia and D. Belardinelli, *Phys. Rev. E* **88**, 013306 (2013).
  - [21] C. S. From, E. Sauret, S. A. Galindo-Torres, and Y. T. Gu, *Phys. Rev. E* **99**, 063318 (2019).
  - [22] X. Shan, *Phys. Rev. E* **77**, 066702 (2008).
  - [23] X. Shan and G. Doolen, *Journal of Statistical Physics* **81**, 379 (1995).
  - [24] K. Küllmer, A. Krämer, W. Joppich, D. Reith, and H. Foyi, *Phys. Rev. E* **97**, 023313 (2018).
  - [25] M. Lulli, R. Benzi, and M. Sbragaglia, *Phys. Rev. X* **8**, 021031 (2018).
  - [26] B. Dollet, A. Scagliarini, and M. Sbragaglia, *J. Fluid Mech.* **766**, 556–589 (2015).
  - [27] G. Falcucci, E. Jannelli, S. Ubertini, and S. Succi, *J. Fluid Mech.* **728**, 362–375 (2013).
  - [28] X. Shan, *Phys. Rev. E* **81**, 036702 (2010).
  - [29] M. L. Porter, E. T. Coon, Q. Kang, J. D. Moulton, and J. W. Carey, *Phys. Rev. E* **86**, 036701 (2012).
  - [30] R. Benzi, M. Sbragaglia, S. Succi, M. Bernaschi, and S. Chibbaro, *J. Chem. Phys.* **131**, 104903 (2009).
  - [31] N. S. Martys and H. Chen, *Phys. Rev. E* **53**, 743 (1996).
  - [32] R. Blossey, *Nature Materials* **2**, 301 (2003).
  - [33] R. Benzi, L. Biferale, M. Sbragaglia, S. Succi, and F. Toschi, *Phys. Rev. E* **74**, 021509 (2006).
  - [34] H. Huang, D. T. Thorne, M. G. Schaap, and M. C. Sukop, *Phys.*

Rev. E **76**, 066701 (2007).

[35] N. K. Andersen and R. Taboryski, *Meas. Sci. Technol.* **28**, 047003 (2017).

[36] X. He, X. Shan, and G. D. Doolen, *Phys. Rev. E* **57**, R13 (1998).

## Appendix A: High-order LB pseudopotential method

In this work, a high-order LB pseudopotential method from our previous work From *et al.* [21] is used. The following provides a summary. In the LB method, mesoscopic representation of fluid flow is described by the distribution function ( $f$ ) where each component ( $\phi$ ) is defined by its own lattice distribution,  $f_\alpha^\phi$ , in configuration space  $\mathbf{x}$ , in each discrete velocity ( $\xi_\alpha$ ) of all directions  $\xi_\alpha : \alpha = 0, \dots, Q$  at time  $t$ . The evolution of  $f$  is defined as

$$f_\alpha^\phi(\mathbf{x} + \xi_\alpha, t + \Delta t) = f_\alpha^\phi(\mathbf{x}, t) - \frac{1}{\tau^\phi} \left[ f_\alpha^\phi(\mathbf{x}, t) + \frac{\Delta t}{2} S_\alpha^\phi(\mathbf{x}, t) - f_\alpha^{eq, \phi}(\mathbf{x}, t) \right] + \Delta t S_\alpha^\phi(\mathbf{x}, t), \quad (\text{A1})$$

where relaxation parameter  $\tau^\phi$  based on the kinematic viscosity  $\nu$  of the fluid, i.e.,  $\nu^\phi = c_s^2(\tau^\phi - 1/2)\frac{\Delta x^2}{\Delta t}$ , where on a discrete lattice  $\Delta x = \Delta t = 1$  and  $c_s$  is the sound speed of the lattice model. In Eq. (A1) the forcing equilibrium distribution (the source term)  $S_\alpha^\phi(\mathbf{x}, t)$  is explicitly coupled to the collision process, which is known as the explicit-forcing (EF) scheme [29, 36]. This source term is defined by [36],

$$S_\alpha^\phi = \frac{\mathbf{F}^\phi(\xi_\alpha - \mathbf{u})}{\rho^\phi c_s^2} f_\alpha^{eq, \phi}. \quad (\text{A2})$$

The discrete equilibrium distribution function up to fourth-order Hermite polynomial expansion is given by (see the seminal work by Shan *et al.* [7]),

$$f_\alpha^{eq} = w_\alpha \rho \left\{ 1 + \underbrace{\frac{\xi_\alpha \cdot \mathbf{u}}{c_s^2}}_{\text{1st order}} + \underbrace{\frac{1}{2} \left[ \frac{(\xi_\alpha \cdot \mathbf{u})^2}{c_s^4} - \frac{u^2}{c_s^2} \right]}_{\text{2nd order}} + \underbrace{\frac{1}{6} \left[ \frac{(\xi_\alpha \cdot \mathbf{u})^3}{c_s^6} - \frac{3u^2(\xi_\alpha \cdot \mathbf{u})}{c_s^4} \right]}_{\text{3rd order}} + \underbrace{\frac{1}{24} \left[ \frac{(\xi_\alpha \cdot \mathbf{u})^4}{c_s^8} - \frac{6u^2(\xi_\alpha \cdot \mathbf{u})^2}{c_s^6} + \frac{3u^4}{c_s^4} \right]}_{\text{4th order}} \right\}, \quad (\text{A3})$$

where  $w_\alpha$  are the lattice weights and sound speed  $c_s$  is specific to the lattice model,  $\sum_\alpha w_\alpha \xi_{\alpha,i} \xi_{\alpha,j} = c_s^2 \delta_{ij}$ . It is reminded that the  $m$ th-order terms recovered in (A3) is dependent on the lattice model. More specifically, for the high-order LB models used in this work, the Q17ZOT [28] and Q25ZOT [9] recover up to third-order terms in (A3), compared to the Q49ZOTT [9, 21] which can recover up to fourth-order terms in (A3).

In Eqs. (A2) and (A3), the term  $\mathbf{u}$  refers to the common mixture velocity and for the EF scheme to conserve momentum

is defined by [29]

$$\mathbf{u} = \frac{\sum_\phi \rho^\phi \mathbf{u}^\phi \omega^\phi}{\sum_\phi \rho^\phi \omega^\phi}, \quad (\text{A4})$$

where  $\omega^\phi = 1/\tau^\phi$ . The macroscopic variables are defined by moments of the equilibrium distribution, i.e., the zeroth and first-order moments are defined respectively by

$$\rho^\phi = \sum_\alpha f_\alpha^\phi, \quad (\text{A5a})$$

$$\rho^\phi \mathbf{u}^\phi = \sum_\alpha f_\alpha^\phi \xi_\alpha + \frac{\Delta t}{2} \mathbf{F}^\phi, \quad (\text{A5b})$$

## Appendix B: Numerical benchmarks and initial conditions

Here details of the numerical benchmarks conducted in this work are provided including the initial conditions and the known theoretical solution to the sinusoidal decay.

### 1. Sinusoidal Decay

In Section I of the main text the sinusoidal decay of a binary mixture was used as benchmark, which has the theoretical solution [24]

$$\begin{aligned} \rho^\phi(\mathbf{x}, t) &= \langle \rho \rangle + \langle \rho \rangle \delta \sin(\lambda x) \exp(-\lambda^2 \mathcal{D}^{\phi\phi} t), \\ \rho^\varphi(\mathbf{x}, t) &= \langle \rho \rangle - \langle \rho \rangle \delta \sin(\lambda x) \exp(-\lambda^2 \mathcal{D}^{\varphi\phi} t), \end{aligned} \quad (\text{B1})$$

where the wave number is given by  $\lambda = 2\pi/n_x$ ,  $\rho(\mathbf{x}) = \rho^\phi(\mathbf{x}) + \rho^\varphi(\mathbf{x})$  and  $\langle \cdot \rangle$  denotes spatial average over the entire space  $\mathbf{x}$  at time  $t$ . Equation (B1) is also used directly to initialize ( $t = 0$ ) density fields  $\rho^\phi(\mathbf{x})$  and  $\rho^\varphi(\mathbf{x})$ , i.e., in (B1) with  $t = 0$  the term  $\exp(-\lambda^2 \mathcal{D}^{\phi\phi} t) = 1$ . A small initial density perturbation is introduced with  $\delta$  and for the tests here is set to  $\delta = 10^{-3}$ . Simulations are conducted on a grid ( $n_x = 200$ ,  $n_y = 4$ ) where at  $x = \frac{1}{4}n_x$  the  $\phi$ -density  $\rho_L^\phi = \rho^\phi(\frac{1}{4}n_x, t)$  with  $\delta = 10^{-3}$  initially ( $t = 0$ ) results in  $\rho_L^\phi - \langle \rho \rangle = 10^{-3}$  for which simulations are run until  $\rho_L^\phi - \langle \rho \rangle = 10^{-6}$  is satisfied.

### 2. Droplet on a Surface

In Section II of the main text a static droplet on a solid surface is simulated, where the droplet (the  $\phi$ -component) in space  $\mathbf{x} = (n_x, n_y)$  are initialized by

$$\rho^\phi(\mathbf{x}) = \frac{\rho_o^\phi}{2} \left\{ (c_H + c_L) - (c_H + c_L) \tanh \left( \frac{2(R^* - R_o)}{W_o} \right) \right\}, \quad (\text{B2})$$

and the surrounding fluid ( $\varphi$ ) by

$$\rho^\varphi(\mathbf{x}) = \frac{\rho_o^\varphi}{2} \left\{ (c_L + c_H) - (c_L + c_H) \tanh \left( \frac{2(R^* - R_o)}{W_o} \right) \right\}. \quad (\text{B3})$$



where  $R_o$  is the initial radius and  $R^* = \sqrt{(x - x_o)^2 + (y - y_o)^2}$  with the location of the droplet defined by coordinates  $x_o$  and  $y_o$ . Simulations are conducted on a symmetric grid ( $n_x = n_y = 200$ ). The top and bottom boundaries are treated as solid nodes with no slip, for which the standard bounce-back [6] boundary condition is applied. Due to streaming, to ensure correct recovery (bounced-back)

distributions on high-order LB models the wall-boundaries are covered by  $\max_\alpha(|\xi_\alpha|)$ -number of layers on the top and bottom. For the lattice models used in this work  $\max_\alpha(|\xi_\alpha|) = 3$ . The droplet is initialized using Eqs. (B2) and (B3) by setting  $x_o = n_x/2$  and  $y_o = R_o + \mathcal{E}_\alpha + 2$  with an initial radius of  $R_o = n_x/4$  and the additional 2 nodes are used to place the droplet just above the bottom wall.